Direct observation of Feshbach enhanced s-wave scattering of fermions

D Genkina[1], LM Aycock[1,2], BK Stuhl[1], H-I Lu[1] and IB Spielman [1]‡

[1]Joint Quantum Institute, National Institute of Standards and Technology, and University of Maryland, Gaithersburg, MD, 20899 USA
[2]Physics Department, Cornell University, Ithaca, NY 14850 USA

E-mail: ian.spielman@nist.gov

Abstract. We directly measured the relative s-wave scattering cross-section of ultracold ^{40}K atoms accross the 20.2 mT Feshbach resonance. We collided a pair of degenerate Fermi clouds and imaged the scattered atoms. Owing to their low density, few atoms scattered, even near the resonance. To optimize signal to noise, we developed techniques to interpret absorption imaging in the regime where the optical intensity changes dramatically as light traverses the cloud, and recoil induced detuning corrections are significant. By applying these techniques to our s-wave scattering data we were able to extract the resonant magnetic field value $B_0 = 20.247(2)$ mT and resonance width $\Delta = 1.0(1)$ mT. These imaging techniques are generally applicable to experimets requiring accurate detection of low atomic densities.

Keywords: Quantum gases, Atomic physics

‡ Corresponding author

1. Introduction

Feshbach resonances are a commonly used technique for tuning the interaction strength in ultracold atomic gases. They have been particularly instrumental in the study of interactions and interaction-dependent processes in cold Fermi gases. Even weak interactions play a crucial role in the physics of atomic Bose-Einstein Condensates (BECs), for example giving rise to their characteristic Thomas-Fermi density profiles [26]. The effects of interactions in Fermi gases, however, are harder to observe. The density of Fermi clouds is typically $\sim$ 1000 times less than that of BECs, making it necessary to enhance the strength of interactions in order to observe them [13]. The tunability of interactions provided by Feshbach resonances has allowed for creation of molecular Bose-Einstein condensates from Fermi gases [9, 12, 30] as well as observation of the phase transition from the BCS to BEC regime at sufficiently low temperatures [1, 3, 22, 31].

A Feshbach resonance occurs when a few-atom bound molecular state energetically approaches the free atomic state [5, 25]. The relative energy of the free atomic states and the molecular state is defined by a bias magnetic field. The Feshbach resonance can thus be approached by changing the bias field. In the simple case where there are no inelastic two-body channels, which is accurate for ^{40}K resonance discussed in this work, the effect of the resonance on the scattering length between two free atoms is [5]

$$a(B) = a_{bg}\left(1 - \frac{\Delta}{B - B_0}\right), \tag{1}$$

where a is the scattering length, a_{bg} is the scattering length away from the resonance, Δ is the width of the resonance, and B_0 is the field value at which the resonance occurs. Note that the scattering length tends to infinity from either side of the resonance.

The exact value of the resonant field B_0 is difficult to calculate analytically and is commonly estimated via numerical models [8, 17, 24] or determined experimentally [6, 10]. Many experimental techniques have been used to characterize Feshbach resonances, including the observation of atom loss due to three-body inelastic scattering, measurement of re-thermalization timescales, and imagin anisotropic expansion of the cloud upon release from a confining potential, all of which infer the elastic scattering cross section from collective behavior of the cloud [19–21].

Here we present a new technique for measuring the location and width of a Feshbach resonance. We collided a pair of ultra-cold Fermi gas clouds and directly imaged the resulting s-wave scattering halo as a function magnetic field strength. This allowed us to observe the enhancement in scattering without relying on proxy effects. We measured the fraction of atoms scattered during the collision, and from this fraction deduced the resonant magnetic field and width of the resonance. A similar technique has been used to characterize impurity scattering in BECs [4].

In our dilute Fermi clouds, even with the resonant enhancement of the scattering cross section, only a small fraction of the atoms underwent a scattering event as the clouds passed through each other. This made direct detection of s-wave scattering halos

difficult due to detection uncertainty, which disproportionately affected regions of low atomic density in absorption images. To optimize the signal to noise for low atom numbers, we utilized a non standard imaging regime. In this regime, the atoms acquire a non-negligible velocity during imaging and are Doppler-shifted away from the light field used to detect them. Simulation of the absorption imaging process was necessary for an accurate interpretation of these images. With the simulation corrected images, we were able to extract the number and the scattered fraction of the atoms.

This paper is in two parts. In the first, we study absorption imaging in the presence of significant time-dependent Doppler shift and show how we use our results to interpret data. In the second, we describe our s-wave scattering experiment and extract a measure of the location and width of the Feshbach resonance in ^{40}K.

2. Absorption imaging in the presence of strong recoil induced detuning

Absorption imaging is commonly thought of as the atomic cloud casting a "shadow" on a camera when illuminated by laser light. This imaging scheme relies on optical transitions between the ground and certain excited atomic states. Such atomic transitions have an energy difference E_0 with an associated frequency $\omega_0 = E_0/\hbar$, and a natural transition linewidth Γ. When interacting with a laser light field an atom will scatter photons: it will absorb a photon from the light field and move up to its excited state, then re-emit the photon and decay back to its ground state. The rate at which this scattering occurs, in the two-level atom approximation, is [18]

$$\gamma_{sc} = \frac{\Gamma}{2}\frac{I/I_{\rm sat}}{1 + (2\delta/\Gamma)^2 + I/I_{\rm sat}}, \tag{2}$$

where $I/I_{\rm sat}$ is the laser intensity as a fraction of the saturation intensity, and δ is the detuning, the difference between the resonant transition frequency ω_0 and the frequency of the laser light ω_L.

An absorption image is obtained by shining an on or near resonant probe beam ($\delta \approx 0$) onto the atomic cloud. Some of the light is scattered by the atoms, and the unscattered light, $I_f(x, y)$, is imaged onto a camera, as seen in Fig. 1a (top). After the atoms leave the imaging volume, the probe light is reapplied to calibrate the intensity $I_0(x, y)$ of light unaffected by the atoms (bottom).

The intensity $I_f(x, y)$ is related to the number of atoms the light encountered. Consider the light as it travels along the imaging axis e_z through a 3-D atomic density profile $\rho(x, y, z)$. For the purposes of this discussion, let us focus on a single pixel of the camera, and thus a single value of I_0 and I_f, and a single column of atoms, $\rho(z)$. We are not able to infer the entire atomic distribution, but for each pixel we can obtain the integrated density, $n = \int \rho\,(z)\ \mathrm{d}z$. As the light travels through a column of atoms, each atom scatters light according to Eq. (2). Therefore, the atoms further along the imaging axis z experience a reduced optical intensity due to attenuation by the other atoms, as seen in Fig. 1b. On resonance ($\delta = 0$), the intensity change from scattering

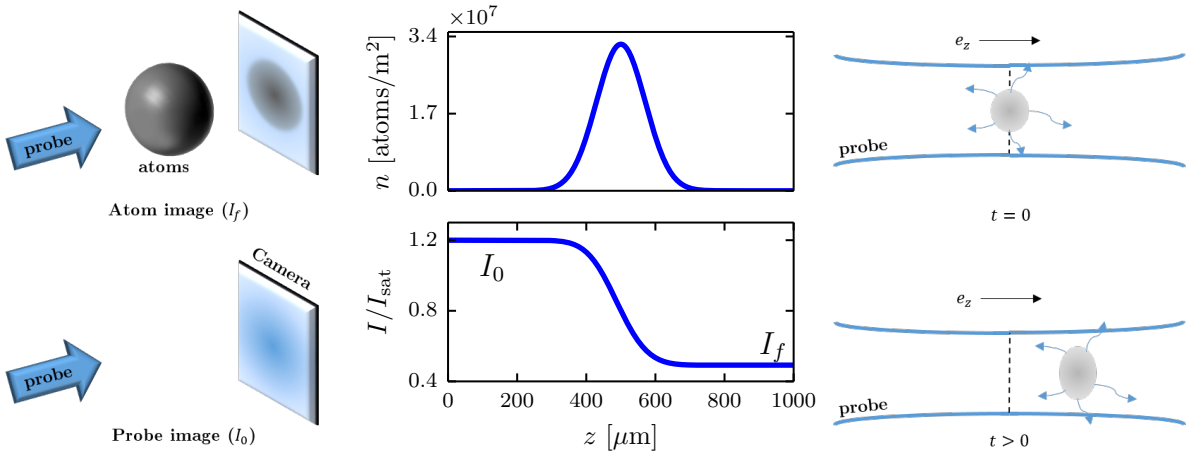

(a) (b) (c)

Figure 1. Absorption imaging. a. Near resonant probe light illuminates the atoms, and the transmitted light (containing a shadow of the atoms) is imaged on the camera. After the atoms depart an image of just the probe light is taken. b. The probe beam is partially absorbed as it traverses the cloud, and the intensity seen by atoms further along the imaging direction $\hat{e}_z$ is lowered. c. An atomic cloud illuminated by a probe light field absorbs photons from the probe and re-emits them in all directions. This process results in a net velocity of the cloud in the direction of the probe light as well as diffusive spreading in the transverse directions.

as a function of z is

$$\frac{dI(z)}{dz} = \hbar\omega_L \rho(z)\gamma_{sc}(z) = -\rho(z)\sigma_0 \frac{I(z)}{1 + I(z)/I_{\rm sat}}, \tag{3}$$

where σ_0 is the resonant scattering cross section. This equation is integrated to obtain [23]

$$\sigma_0 n = -\ln\left(\frac{I_f}{I_0}\right) + \frac{I_0 - I_f}{I_{\rm sat}}. \tag{4}$$

In the limit where the probe intensity is much smaller than the saturation intensity, $I_0 \ll I_{\rm sat}$, this reduces to the optical depth, $OD_0 = -\ln(I_f/I_0)$ [23]. This is the simplest possible model that relates the observed intensities to the column density n. When the probe intensity is comparable to the saturation intensity, the second term in Eq. (4) becomes significant, and we define the optical density corrected for high probe intensity OD_1 as the right hand side of Eq. (4).

There are further corrections that this equation does not take into account. In particular, it neglects the atomic recoil momentum and its effect on the laser detuning [14]. When an atom absorbs a photon from the laser light field and is excited to a higher energy level, by conservation of momentum it must also acquire a velocity increment in the direction of the light field. This recoil velocity is given by $v_r = \hbar k/m$, where

$k = 2\pi/\lambda$ is the wavenumber of the light field with wavelength λ and m is the atomic mass. When the atom returns to its ground state, the photon is re-emitted with some momentum $\vec{p}_e$. Over many photons, this momentum distribution averages to zero, $\int \vec{p}_e \mathrm{d}^3x = 0$. Therefore, on average, the atom will acquire a net velocity of v_r in the $\hat{e}_z$ direction. The variance of $\vec{p}_e$, however, is not zero, allowing the atoms to acquire some momentum transverse to the laser field. We will ignore this correction, but the effect of this on the atomic cloud is pictured in Fig. 1c.

Once the atoms absorb enough photons that they acquire a substantial velocity in the direction of the light field, this velocity Doppler shifts them away from resonance with the light field. After scattering N photons an atom acquires an average velocity Nv_r and an additional detuning $\delta = kNv_r$. Therefore, even if the probe beam is initially on resonance with the atomic transition, we cannot neglect the detuning term in the scattering rate as time goes on. Furthermore, this detuning varies both with imaging time t and with distance along the propagation direction z (Fig. 2a). Thus, the intensity lost to the atoms also acquires a time dependence:

$$\frac{dI(t,z)}{dz} = \sigma_0 \rho \frac{I(t,z)}{1 + [2\delta(t,z)/\Gamma]^2 + I(t,z)/I_{\mathrm{sat}}}, \tag{5}$$

where the detuning δ is

$$\delta(t,z) = \frac{v_r}{\hbar c \rho} \int_0^t \frac{dI(z,\tau)}{dz}\, \mathrm{d}\tau; \tag{6}$$

the relationship between the atomic density and the observed intensities is no longer straightforward.

By considering this equation perturbatively in time we obtain corrections to second order in imaging time [15]

$$\sigma_0 n \approx OD^{(0)} + OD^{(1)} t + OD^{(2)} t^2 = OD_2 \tag{7}$$

$$OD_2 = OD_1 + \frac{(kv_r t)^2}{3} \left[\frac{I_{\mathrm{sat}}}{I_f + I_{\mathrm{sat}}} - \frac{I_{\mathrm{sat}}}{I_0 + I_{\mathrm{sat}}} + \ln\left(\frac{I_f + I_{\mathrm{sat}}}{I_0 + I_{\mathrm{sat}}} \right) \right]. \tag{8}$$

However, as shown in Fig. 2b, the perturbative treatment breaks down shortly after the zeroth order approximation of Eq. (4). To adequately correct for the recoil induced detuning of the atoms, we numerically simulated the imaging process to obtain I_f as a function of imaging time, atomic density, and probe intensity.

In the following, we describe two versions of this simulation. First, we took a simplistic approach where the spatial distribution of atoms does not change appreciably during the imaging time: $vt \ll I_0/(\hbar\omega_L \gamma_{sc} \rho)$. We tested this approach in known limits and then checked the validity of the static assumption. For realistic input parameters, we found this assumption to be invalid. We developed aquasi-classical approach and allowed the atoms to move during the imaging time, allowing us to simulate the phase space evolution of atoms subjected to probe light. While the atomic trajectories were wildly different than in the static atom approximation, the predicted ODs only varied on the 0.5% level between the two models.

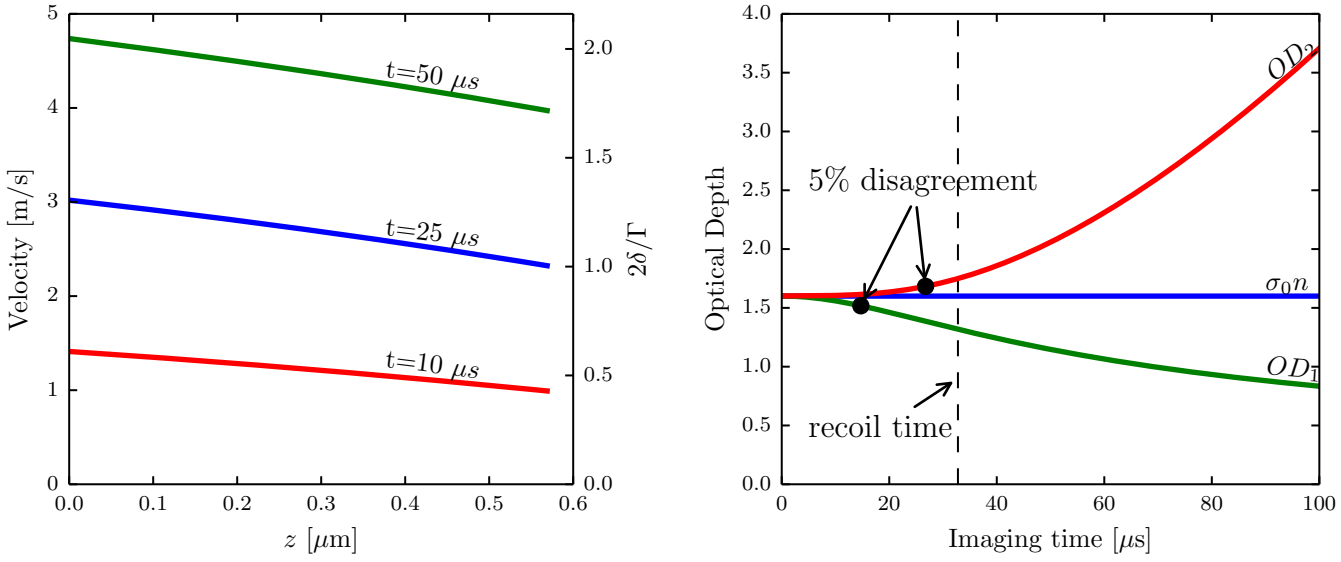

(a) (b)

Figure 2. (a) Dependence of velocity and detuning on position along the imaging axis in an atomic cloud of ^{40}K for three different imaging times and a probe intentisy $I_0 = 1.5 I_{\rm sat}$, as obtained by numerical simulation. (b) Using time dependent I_f values obtained from recoil detuning corrected simulation of on-resonant imaging of ^{40}K atoms at probe intensity $I_0 = 0.8\, I_{\rm sat}$, this graph shows the optical depths obtained by each model. The 'true' optical depth is $\sigma_0 n = 1.6$. OD_1 is the high probe intensity corrected optical depth given by Eq. (4). OD_2 is the high probe intensity corrected and expanded to second order in time optical depth, Eq. (8) [15]. The recoil time is the time it takes for the cloud, on average, to become detuned by a linewidth Γ. Both models start to differ from the true value before a recoil time.

2.1. Stationary atom model

To solve Eqs. (5)-(6), we started with a 1-D distribution of atomic densities $\rho(z)$, assumed to be Gaussian in shape. We divided the cloud into spatial bins (the bin size was decreased until the result only differed at the 10^{-5} level from smaller bin sizes). In this approximation, we kept the number of atoms in each bin constant. The algorithm used is shown in Alg. [1]. We call the optical depth obtained from this algorithm the 'corrected' optical depth, OD_{corr1}.

We checked the validity of our simulation in the limits where the problem is analytically solvable. In the limit where the probe intensity is much weaker than the saturation intensity, $I_0 \ll I_{\rm sat}$, the atoms' velocity is hardly changed, and Eq.(5) reduces to

$$\frac{dI(z)}{dz} = -\rho\sigma_0 I(z), \tag{9}$$

Algorithm 1 Stationary atom model

$I[n=0,t] = I_0$ {n is the bin index, t is the time index, I is in units of $I_{\rm sat}$}
$\delta[n,t=0] = 0$ {light initially resonant, δ in units of $\Gamma/2$}
$I_f = 0$ {no light has entered the cloud}
for $t = 0$ to t_f **do** {loop over time steps}
  for $n = 1$ to N **do** {loop over bins, N is total bin number}
    $A = \sigma_0 \rho[n] dz$ {dz is the size of spatial step}
    $B = v_r dt/(\hbar c \rho[n])$ {dt is the size of the time step}
    $I[n,t] = I[n-1,t] - AI[n-1,t]/(1 + \delta[n,t-1]^2 + I[n-1,t])$ {Eq. (5)}
    $\delta[n,t] = \delta[n,t-1] + B\,(I[n-1,t] - I[n,t])$ {Eq. (6)}
  end for
  $I_f = I_f + I[N,t]dt$ {collecting total fluence seen by the camera}
end for
$OD_{corr1} = -\ln(I_f/I_0 t_f)$

from which we recover the analytic form

$$\sigma_0 n = OD_0 = -\ln I_0/I_f. \tag{10}$$

In the limit that the probe intensity is much stronger than the saturation intensity, $I_0/I_{\rm sat} \gg \delta/2\Gamma$, even far detuned atoms will absorb light at their maximum. The time dependence of the detuning can thus be neglected, and Eq. (5) becomes

$$\frac{dI(z)}{dz} = -\rho\sigma_0 I_{\rm sat}, \tag{11}$$

which integrates to

$$\sigma_0 n = \frac{I_0 - I_f}{I_{\rm sat}}. \tag{12}$$

We recognize the right hand sides of Eq. (10) and Eq. (12) as the two terms in the expression for OD_1 in Eq. (4). Thus, as shown in Fig. 3, in both limits OD_{corr1} coincides with OD_1 in both the small and large probe intensity limits.

We used the results of this simulation to check if the stationary atom assumption is valid, i.e. if the distance traveled by the atoms as deduced from integrating the acquired recoil velocity over the imaging time is less than the bin size. As can be seen from Fig. 4a, not only do the atoms travel more than the bin size, but they travel far beyond the initial extent of the cloud. Moreover, owing to the high scatter rate, the back of the cloud overtakes the front for long imaging times. Thus, the atomic distribution as a function of position changes dramatically during the imaging pulse, and the stationary assumption is invalid.

2.2. Traveling atom model

To account for the changing atomic distribution during the imaging pulse, we numerically simulated the classical kinetics of atoms subject to the recoil driven optical

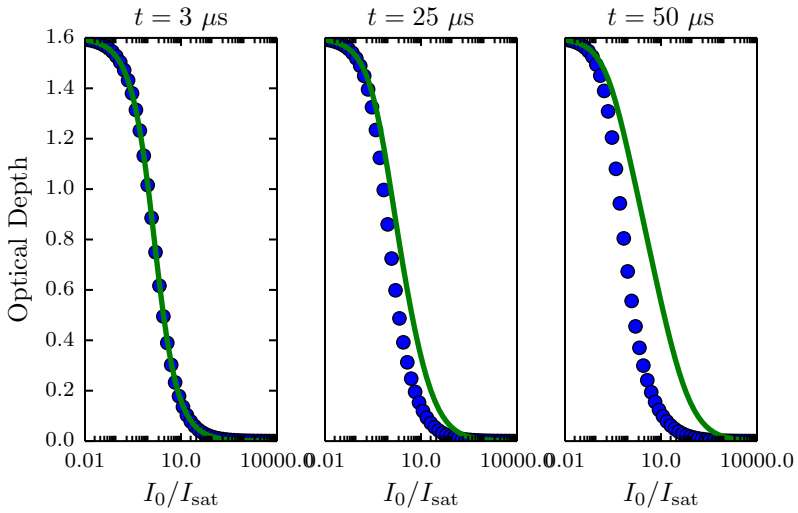

Figure 3. Optical depth as a function of probe intensity as predicted by the simulation (blue symbols) and by Eq. (4) (green curves), for three different imaging times. The predictions agree in both the high and low intensity limits, and differ for probe intensities comparable to the saturation intensity and longer imaging times.

forces. To simulate large ensembles in a reasonable time, composite atoms described the aggregate behavior of N_{ca} atoms. The amended algorithm is shown in Alg.[2].

To validate our code, we checked the velocity predicted in this model against known limits. One such limit is that of a singlecomposite atom. In this case, there is no attenuation, and the intensity seen by the composite atom is constant at I_0. Only the detuning evolves in time, and Eqs. (5) and (6) give

$$\frac{dD(t)}{dt} = k_R v_r \frac{\tilde{I}}{1 + D^2 + \tilde{I}}, \tag{13}$$

where $D = 2\delta/\Gamma$, and $\tilde{I} = I_0/I_{\rm sat}$. Equation (13) can be solved numerically, and is in good agreement with our simulation, as seen in Fig. 4b.

We used this model to study the time evolution of the cloud shape during imaging and visualized the phase space evolution of superatoms, shown in Fig. 5. The cloud shape is strongly distorted during the imaging time.

We compared the optical depths predicted by each of the two models, OD_{corr1} and OD_{corr2}. As seen Fig. 6a, the predicted optical depths were hardly changed by including the full time evolution: $|OD_{corr1} - OD_{corr2}|\,/OD_{corr1} \leq 0.005$. Thus, for the purposes of deducing the atom density from experimental optical depths, the stationary atom model is sufficient. Furthermore, we simulated a range of initial density profiles $\rho(z)$, and found their impact to be negligible – the only observable is the integrated atomic density $n = \int \rho(z) \mathrm{d}z$. For interpreting experimental images, we used the data generated by the travelling atom simulation.

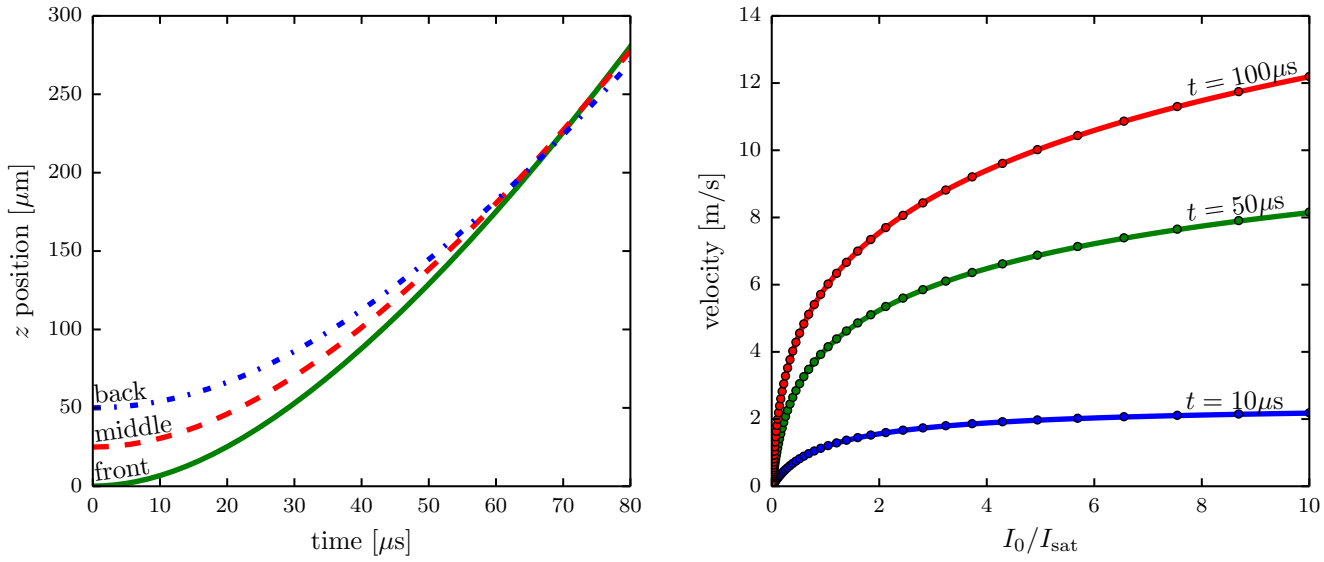

(a) (b)

Figure 4. (a) Position of atoms as a function of imaging time for atoms in the first (solid green), middle (dashed red), and last (dotted blue) bins of the simulation for an initial cloud 50 μm in extent, obtained by integrating their velocities. The probe intensity used in this calculation is $1.2\,I_{\rm sat}$, and the optical depth is 1.6. (b)The velocity of a single superatom as a function of probe intensity for various imaging times. Simulation data (dots) and numerical solutions of Eq. (13) (lines) are in good agreement.

2.3. Signal to noise optimization

This simulation allowed us to interpret experimentally obtained final intensities. For a given imaging time, we created a look-up table of predicted optical depth as a function of probe intensity and atomic density. We then found the observed optical depth on this table, with the given probe intensity, and inferred the atomic density. The uncertainty in the measured intensities can be propagated through this procedure, and we established optimal imaging parameters to maximize the signal to noise ratio of this detection scheme.

Here, the only source of measurement uncertainty we considered was the Poisson distributed photon shot noise, with a standard deviation proportional to $\sqrt{N_p}$, where N_p is the photon number. We then propagated this uncertainty through our correction scheme to obtain the uncertainty in our deduced value of $\sigma_0 n$. We define the signal to noise ratio (SNR) as $\sigma_0 n/\delta_{\sigma_0 n}$, where $\delta_{\sigma_0 n}$ is the propagated measurement uncertainty.

As seen in Fig. 7a, after about 40 μs extending the imaging time no longer yields appreciable improvement in SNR. Imaging for 40 μs as opposed to 10 μs where the

Algorithm 2 Travelling atom model

$z[n] = z_0$, $\delta[n] = 0$ {initialize position and detuning for each composite atom, labeled by index n}
$O[i] = n$ {make a list of composite atom indexes, ordered by position}
$I[n = 0, t] = I_0$ { t is the time index, I is in units of I_{sat}}
$I_f = 0$
for $t = 0$ to t_f **do** {loop over time steps}
  for $i = 1$ to N **do** {loop over superatoms}
    $n = O[i]$ {apply probe intensity to composite atoms in order of appearance}
    $A = \sigma_0 N_{sa} dz$ {dz is length over which atoms were grouped into single composite atom}
    $B = v_r dt/(\hbar c N_{sa})$ {dt is the time step}
    $I[n, t] = I[n-1, t] - AI[n-1, t]/(1 + \delta[n]^2 + I[n-1, t])$ {Eq. (5)}
    $\delta[n]$ += $B\,(I[n-1, t] - I[n, t])$ {Eq. (6), detuning in units of $\Gamma/2$}
    $z[n]$ += $dt\Gamma\delta/2k$ {k is the wavenumber, $\Gamma\delta/2k$ is the velocity at δ detuning}
  end for
  $O[i]$=sort(n, key =$z[n]$) {sort composite atom indexes by current position}
  $I_f = I_f + I[N, t]dt$ {collecting total fluence seen by the camera}
end for
$OD_{corr2} = -\ln(I_f/I_0 t_f)$

uncorrected model is appropriate, improves the SNR by a factor of 1.5. We performed the experiments described in the second section at 40 μs imaging time. Figure 7b shows that the optimal probe intensity varies with the magnitude of ODs. For low atom numbers, $OD \approx 0.1$, a probe intensity of $I_0 \approx 0.6\, I_{\text{sat}}$ is best. However, in our experiment the probe intensity had a gaussian profile and was not uniform over the whole image. The typical probe intensities used in our experiments varied over the $I_0 = 0.1\, I_{\text{sat}} - 0.7\, I_{\text{sat}}$ range.

2.4. Calibration of saturation intensity

A charge-coupled device (CCD) camera was used to take the absorption images. Each camera pixel converts the photons it is exposed to, with some efficiency, into photoelectrons, and digitally outputs an integer, called 'counts', that is proportional to the photoelectrons. However, the proportionality constant depends on many factors, such as the quantum efficiency of the camera, the electronic gain during the readout process, and the polarization of the probe light.

We determined this proportionality constant through direct measurement. In the limit where the system is adequately described by the uncorrected OD_0, only the ratio of the initial and final intensities matter, and this proportionality constant is irrelevant. In all other regimes, however, the ratio of the initial and final intensities to the saturation intensity also comes into play, making the proportionality constant significant. One

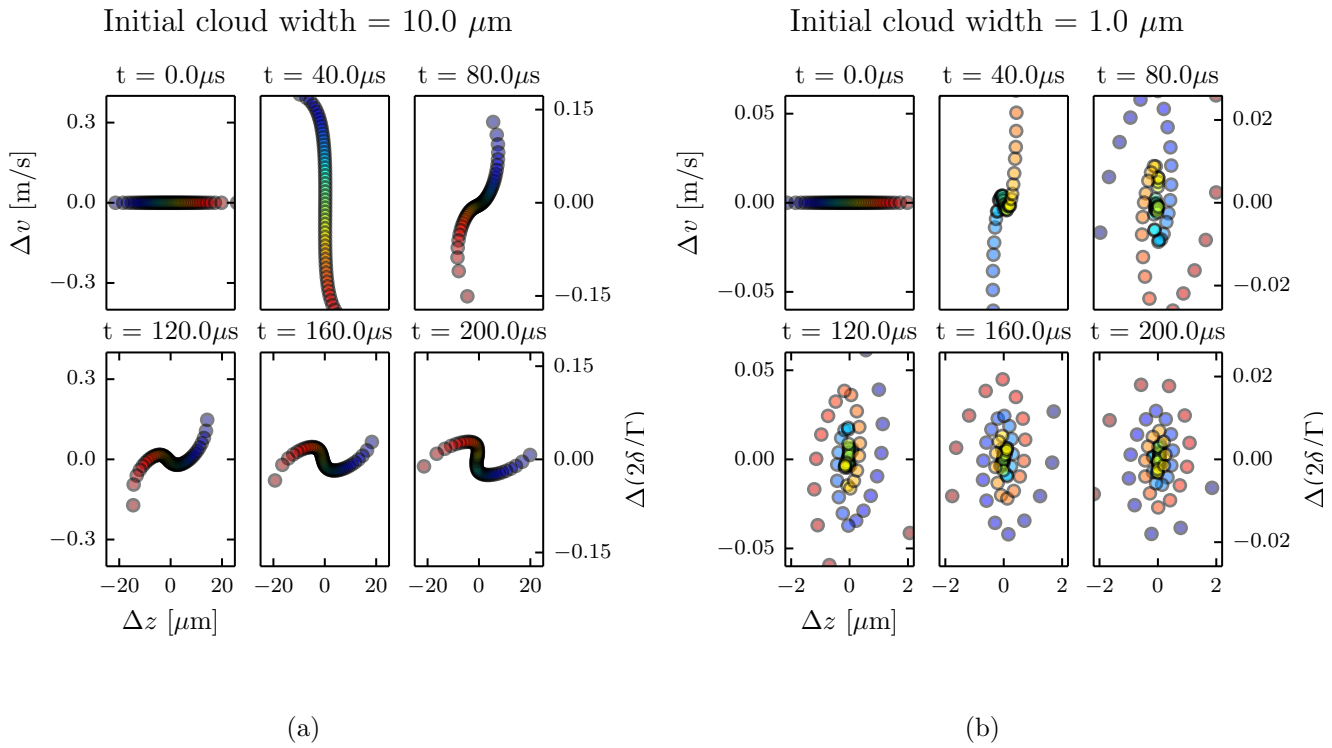

Figure 5. Phase space evolution of an atomic cloud exposed to probe light with intensity $I_0 = 1.2\, I_{\rm sat}$. We defined $\Delta v = v - \langle v(t)\rangle$, $\Delta(2\delta/\Gamma) = 2\delta/\Gamma - \langle 2\delta(t)/\Gamma\rangle$ and $\Delta z = z - \langle z(t)\rangle$, subtracting out the center of mass position, velocity and detuning of the cloud. The optical depth is 1.6, and the initial cloud is a gaussian with a width of 10 μm in (a) and 1 μm in (b). The center of mass detunings $\langle 2\delta(t)/\Gamma\rangle$ are (0, 1.47, 2.26, 2.81, 3.23, 3.58) sequentially, and are the same for both initial cloud widths.

way to approach this calibration is to determine the value of the saturation intensity in 'counts' per unit time.

To calibrate the saturation intensity in camera counts per unit time, we took absorption images of a cloud of ^{40}K atoms at three different imaging times, 40 μs, 100 μs, and 200 μs, at varying probe intensities. In a small region at the center of the cloud the atomic density is approximately uniform, and we averaged the initial and final intensities of each pixel in that region. Thus, for each image we obtained I_0 and I_f, in counts per microsecond. We then did a least squares fit of OD_{corr}, our simulated optical depth, to the data at all three imaging times simultaneously. The two fit parameters were the atomic density n at the center of the cloud and the value of $I_{\rm sat}$ in counts per microsecond. As seen in Fig. 6b, the model produced a good fit to the experimental data, and we obtained a calibration of the saturation intensity for our experiment.

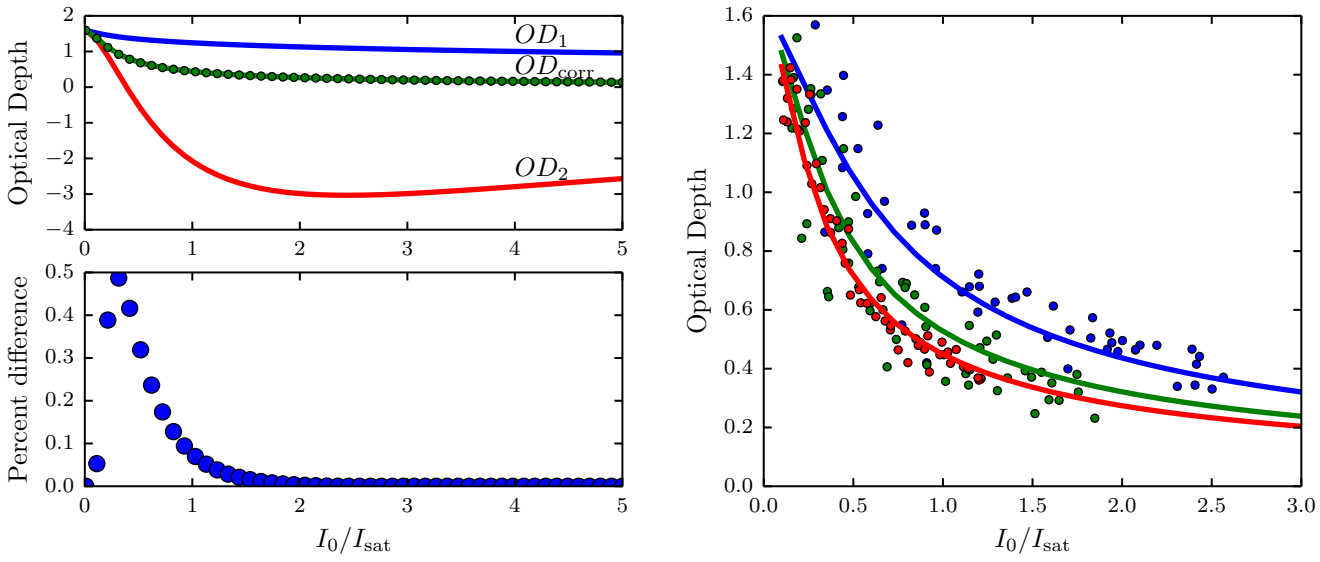

(a) (b)

Figure 6. (a) Top. Optical depth as a function of probe intensity for an imaging time $t = 100$ μs. The two versions of simulated optical depth, OD_{corr1} (green curve) and OD_{corr2} (green dots) are plotted. Bottom. The percent difference, $100 * |OD_{corr1} - OD_{corr2}|/OD_{corr2}$, from the top graph. (b) The optical depth as a function of probe intensity for three imaging times: $t = 40\mu$s (blue), $t = 75\mu$s (green), $t = 100\mu$s (red). The dots represent experimental data and the lines represent the best fit of simulated data. The optimal fit parameters pictured are a $\sigma_0 n$ of 1.627(5) and saturation intensity of 29(7) counts/μs.

3. S-wave scattering experiment

In this section we describe our Fermi scattering experiment. We scattered two counter-propagating ^{40}K clouds and observed the resulting s-wave halo of scattered atoms. We measured the dependence of the scattered atomic fraction on the bias magnetic field in the vicinity of the Feshbach resonance. We used this data to extract the location of the magnetic fields resonance of 20.247(2) mT and a width of 1.0(1) mT, similar to the accepted values of 20.210(7) mT and 0.78(6) mT [22].

3.1. Experimental procedure

We prepared clouds of cold ^{40}K atoms in a hybrid ^{40}K and ^{87}Rb apparatus, previously described in [11, 16, 27]. We used a Zeeman slower to sequentially slow both species before being captured in a magneto-optical trap (MOT) allowed both species to cool in optical molasses for 2 miliseconds. We optically pumped both species into a magnetically

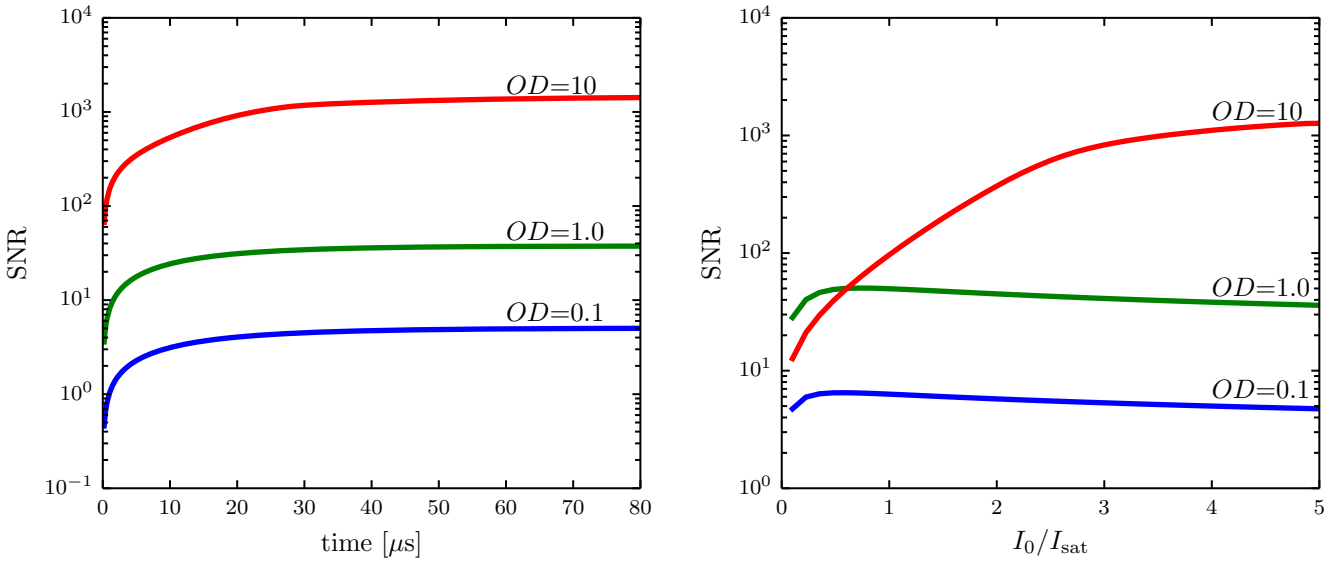

Figure 7. Signal to noise ratio (SNR) for three different optical depths after correcting for recoil induced detuning. (a) SNR as a function of probe intensity $I_0/I_{\rm sat} = 5.0$ and (b) SNR as a function of probe intensity for an imaging time of 50 μs.

trappable state, $|F = 9/2, m_F = 9/2\rangle$ for ^{40}K and $|F = 2, m_F = 2\rangle$ for ^{87}Rb. Both species were then loaded into a quadrupole magnetic trap, and cooled evaporatively. The magnetic trap was plugged by a tightly focused green beam at the center, providing a repulsive potential around the zero field point to prevent Majorana losses. Since the ^{40}K atoms are dilute and only interact very weakly with each other, they re-thermalize primarily due to interaction with ^{87}Rb atoms, and therefore the ^{87}Rb atoms are necessary to evaporatively cool ^{40}K. We then load the atoms into a crossed optical dipole trap, with trap frequencies of $(\omega_x/2\pi, \omega_y/2\pi, \omega_z/2\pi) = (39, 42, 124)$ in the three spatial directions. We continued evaporative cooling by slowly ramping down the dipole trap. We then used adiabatic rapid passage (ARP) to transfer the ^{87}Rb atoms from the $|F = 2, m_F = 2\rangle$ state to the $|F = 1, m_F = -1\rangle$ absolute ground state. This state was chosen to minimize spin changing collisions with ^{40}K atoms during any further evaporation [2]. We then briefly applied an on-resonant probe laser, ejecting any remaining ^{87}Rb atoms in the $F = 2$ manifold from the trap. We again used ARP to transfer the ^{40}K atoms into an equal superposition of $|F = 9/2, m_F = -9/2\rangle$ and $|F = 9/2, m_F = -7/2\rangle$, and further evaporated in the dipole trap [7]. Since ^{87}Rb is heavier than ^{40}K, we were able to evaporate the ^{40}K atoms past the point where ^{87}Rb atoms were no longer suspended against gravity and fell out of the dipole trap. These

hyperfine states of ^{40}K were then used to study their Feshbach resonance.

We ramped the bias field in a two-step fashion to the desired value B near the Feshbach resonance. We approached the field using a large pair of coils in Helmholtz configuration to bring the magnetic field to a setpoint 0.59 mT away from B. We held the atoms at this field for 100 ms to allow the eddy currents induced by the large coils to settle, and then used a lower inductance (smaller) set of Helmholtz coils to quickly change the field the remaining 0.59 mT. We took two sets of data: one approaching the resonance from below, where we used the large coils to get the field to $B - 0.59$mT and used the small coils to quickly get to the desired field, and one coming from above the resonance, where we used the large coils to get to $B + 0.59$mT and then used the small coils to quickly get the field down to the desired value. This allowed us to study the resonance from both sides without the added losses associated with going through the resonance [5].

The magnetic field B was independently calibrated by pulsing on a pre-set radio frequency signal and finding the large coil current setting that optimally transferred ^{40}K atoms in $|F = 9/2, m_F = -9/2\rangle$ to an equal superposition of $|F = 9/2, m_F = -9/2\rangle$ and $|F = 9/2, m_F = -7/2\rangle$ via fast oscillation in the small coils causing decoherence.

Once we had the Fermi cloud at the intended bias field, we split the cloud into two spatially overlapping components with momenta $p = \pm 2\hbar k_L$ and observed scattering as they moved through each other and separated. To create these counterpropagating components, we used a double pulse sequence [29] of a near resonant (λ_L=766.704 nm) 1-d retro-reflected optical lattice. The pulse sequence was optimized to transfer most of the atoms into the $\pm 2\hbar k_L$ momentum states, where k_L is the recoil momentum of the lattice. Since the initial Fermi gas had a wide momentum spread (in contrast to a BEC, which has a very narrow momentum spread), and the lattice pulsing is a momentum dependent process, not all the atoms were successfully transferred into the target momentum states. We optimized our pulse times to minimize the atoms remaining in the zero momentum state. The optimized pulse times were 23 μs for the first square pulse, 13 μs off interval, and 12 μs for the second square pulse. An $8E_L$ lattice was used, where $E_L = \hbar^2 k_L^2 / 2m_K$ is the lattice recoil energy.

We then released the atoms from the trap and allowed 1 ms for the two opposite momentum states within the cloud to pass through each other, scattering on the way. For the data taken coming from below the Feshbach resonance, we then simply ramped down the field and imaged the atoms. For the data taken coming from above the Feshbach resonance, we ramped the field back up, retreating through the resonance if it had been crossed and thereby dissociating any molecules that were created, and then quickly ramped the field back down and imaged the atoms. We used a 40 μs imaging pulse with $I_0/I_{\rm sat} \approx 0.6$ at the center.

The total time-of-flight, the time from the moment the atoms were released from the trap to when they were imaged, was $t_{TOF} = 6.8$ ms. In such an image, observed atomic position is determined by the distance traveled during t_{TOF}, which is determined by its initial velocity when it was released from the trap. Therefore, this technique measures

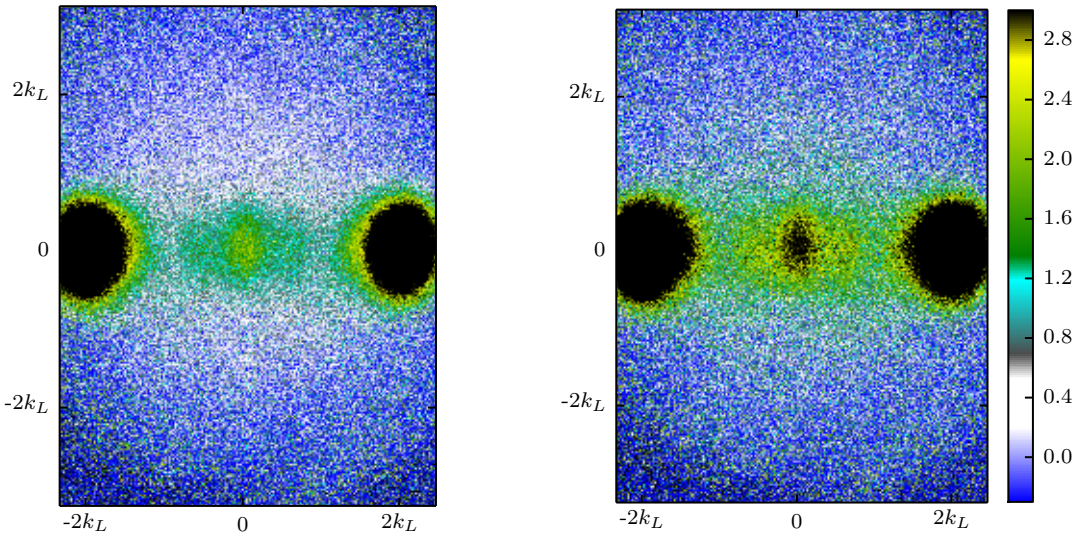

Figure 8. An example of our absorption image after 6.8 ms time of flight. The 1-D lattice imparts momentum along e_x. The two large clouds on the left and right are the atoms in the $\pm 2k_r$ momentum orders that passed through each other unscattered. The smaller cloud in the center is the atoms that remained in the lowest band of the lattice after pulsing, and thus obtained no momentum. The thin spread of atoms around these clouds is the atoms that underwent scattering. This image was taken coming from below the Feshbach resonance at 20.07 mT. (a) Raw optical depth, (b) corrected optical depth.

the momentum and not the position distribution of the atoms.

3.2. Methods

We first corrected each image for recoil induced detuning as described in the previous section. An example of this correction procedure is shown in Fig. 8. To improve the signal and compensate for any shot to shot number fluctuations, we took 15 nominally identical images for each data point and averaged the corrected OD images.

We counted the fraction of atoms that experienced a single scattering event as a function of the bias field. Single scattering events are easily identified, as two atoms that scatter elastically keep the same amplitude of momentum, but align along an arbitrary direction. Therefore, an atom traveling at $2\hbar k_L$ to the right that collides ellastically with an atom traveling at $2\hbar k_L$ to the left will each depart with a momentum of $2\hbar k_L$ in opposite directions at an arbitrary angle to the initial collision axis, and in a time of flight image such atoms will lie in a spherical shell centered on the center of mass, producing the scattering halo pictured in Fig. 9a.

Absorption images captured the integrated column density along e_z, a projected

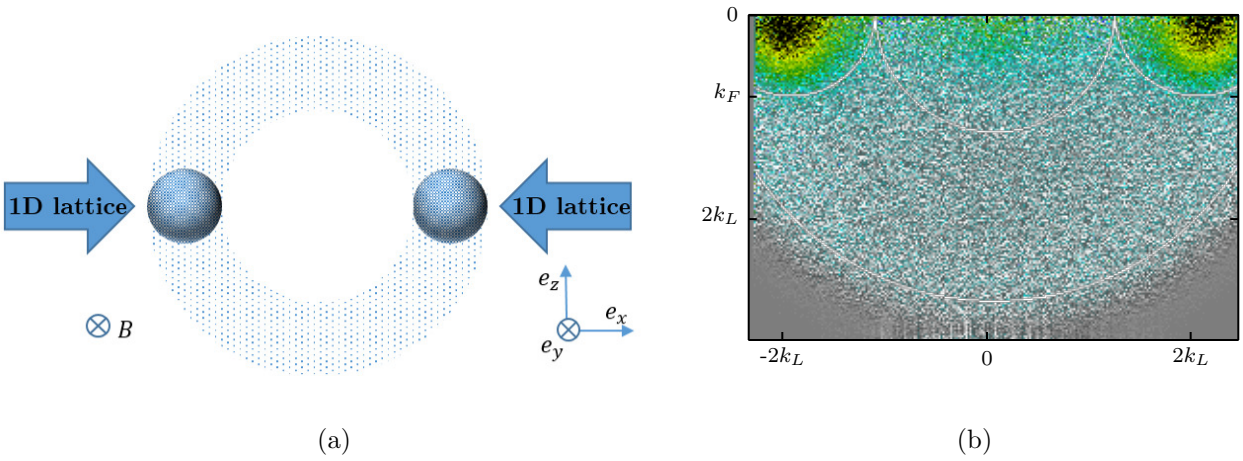

(a) (b)

Figure 9. (a) Our experimental setup. After time of flight, the two clouds traveling along $\pm\hat{e}_x$ directions have separated and the atoms that underwent a single scattering event were evenly distributed in a scattering halo around the unscattered clouds. The 1-D lattice defined the axis of cylindrical symmetry. (b) Inverse Abel transformed image. The atoms within the Fermi momentum k_F of each unscattered cloud center are in the unscattered region and counted towards the total unscattered number. The atoms outside the radius $k_r - k_F$ but inside $k_r + k_F$ but outside the unscattered region are counted towards the number of single scattered atoms.

2-D atomic distribution. To extract the radial dependence of the 3-D distribution from the 2-D image, we performed a standard inverse Abel transform. The inverse Abel transform assumes cylindrical symmetry, which was present in our case, with the axis of symmetry along e_x, defined by the lattice. We thus obtained the atomic distribution as a function of r, the radial distance from the scattering center, and θ, the angle between r and symmetry axis e_x, integrated over ϕ, the azimuthal angle around the x axis.

We then extracted the number of scattered atoms N_{scat} as a fraction of the total atom number N_{tot} for each bias magnetic field, as shown in Fig. 9b.The unscattered atom numberwas the number of atoms in the two unscattered clouds. The number of atoms that underwent a single scattering event was the number of atoms outside the Fermi radius of the unscattered clouds, but inside the arc created by rotating the Fermi momentum k_F around the original center of the cloud (white arcs in Fig. 9b). The total atom number in the image was the sum of those two. The atoms in the center region were not counted as they were originally in the zero momentum state and could not contribute to the scattering halo we were looking for.

We then used our data to deduce the resonant field value B_0 and width of the resonance Δ, the parameters in Eq. (1). Since we were in the low energy regime (the thermal deBroigle wavelength was much larger than the range of inter-atomic van der Waals interactions $\lambda_{dB} \gg l_{vdW}$ [28]), the scattering cross-section was given by $\sigma = 4\pi a^2$.

One way to think about the scattering cross-section σ is that the probability P_{scat} that a single particle will be scattered when incident on a cloud of atoms with

a surface density of N/A is given by $P_{scat} = \sigma N/A$. In our case, half the initial cloud, with atoms number $N_{tot}/2$, is incident on the other half of the initial cloud, again with $N_{tot}/2$ atoms. Thus, the number of scattered atoms should be given by $N_{scat} = (N_{tot}/2)\sigma(N_{tot}/2) = \sigma N_{tot}^2/4A$, where A is the cross-sectional area of the cloud. Assuming A is constant for all our data, we can absorb the factor of 4A into our definition of a_{bg}, along with the 4π, to obtain the fit function

$$\frac{N_{scat}}{N_{tot}^2} = \tilde{a}_{bg}^2 \left(1 - \frac{\Delta}{B - B_0}\right)^2 + C. \tag{14}$$

We found that our imaging noise skewed towards the positive, giving rise to a small background offset. We accounted for this in our fit by including a constant offset parameter C.

3.3. Results

Our final data is presented in Fig. 10. The red curve depicts a best fit of the model given in Eq. (14). The fit parameters we extracted were $\Delta = 1.0(1)$ mT, $B_0 = 20.247(2)$ mT, and $C = 9.00e-5$. The error bars on the fitted data were obtained solely from photon shot noise of both absorption images propagated through our analysis. The accepted values for the ^{40}K s-wave Feshbach resonance for the $|9/2, -9/2\rangle$ and $|9/2, -7/2\rangle$ states are $B_0 = 20.210(7)$ mT and $\Delta = 0.78(6)$ mT [22]. The difference in our measurement may be a result of scattering with atoms that did not receive a momentum kick from the lattice pulsing, a process that was not taken into account by our analysis, or impact of multiple scattering events.

4. Conclusion

We studied the effects of recoil-induced detuning effects on absorption images and found an optimal imaging time of ≈ 40 μs for ^{40}K atoms for noise minimization after corrections. We use these results to observe s-wave scattering halos of the Fermi gas around the Feshbach resonance and directly verify the resonance location and width. Our analysis can be used in any absorption imaging application where signal to noise minimization is critical. We performed a new kind of measurement of the resonant magnetic field and width of a Feshbach resonance.

Acknowledgments

We thank Marcell Gall for helpful discussions. This work was partially supported by the AROs Atomtronics MURI, by the AFOSRs Quantum Matter MURI, NIST, and the NSF through the PFC at the JQI. B.K.S. is a NIST-NRC Postdoctoral Research Associate. L.M.A. was supported by the NSF GRFP.

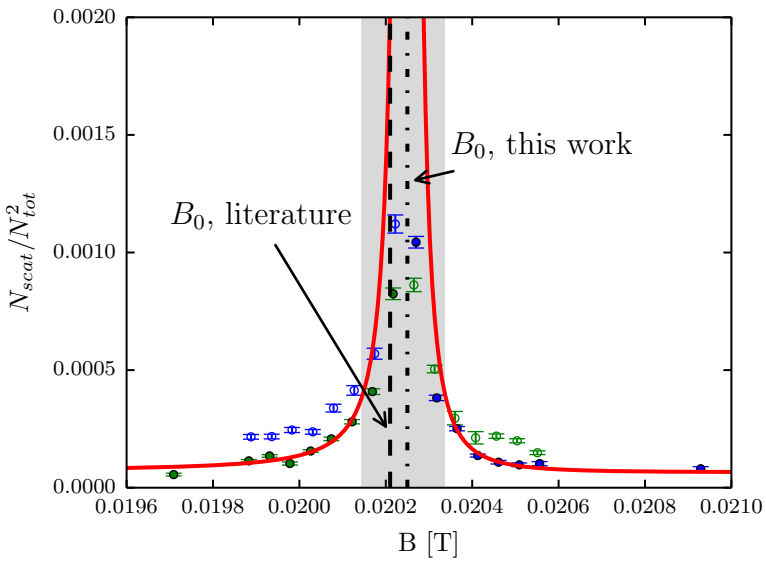

Figure 10. Normalized scattered population plotted versus bias field B. Green dots represent data taken coming from below the resonance, and blue dots represent the data taken coming from above the resonance. The red curve depicts the best fit, where data coming from above the resonance was used above the resonance and data coming from below the resonance was used below the resonance to create the fit; the unused data points are indicated by hollow dots. The regime where the scattering length is likely large enough for the atoms to behave hydrodynamically is shaded in gray. Data points in that region were not used in the fit, as there the assumption $\sigma\rho \ll 1$, where ρ is the atom number per unit area, is no longer valid. Values for the resonant field B_0 from literature and as found in this work are indicated.

References

[1] M. Bartenstein, A. Altmeyer, S. Riedl, S. Jochim, C. Chin, J. Hecker Denschlag, and R. Grimm. Collective excitations of a degenerate gas at the bec-bcs crossover. *Phys. Rev. Lett.*, 92:203201, 2004.

[2] Thorseten Best. *Interacting Bose-Fermi mixtures in optical lattices.* PhD thesis, Johannes Gutenberg-Universitat, 2010.

[3] T. Bourdel, L. Khaykovich, J. Cubizolles, J. Zhang, F. Chevy, M. Teichmann, L. Tarruell, S. J. J. M. F. Kokkelmans, and C. Salomon. Experimental Study of the BEC-BCS Crossover Region in Lithium 6. *Phys. Rev. Lett.*, 93:050401, 2004.

[4] A. P. Chikkatur, A. Görlitz, D. M. Stamper-Kurn, S. Inouye, S. Gupta, and W. Ketterle. Suppression and enhancement of impurity scattering in a Bose-Einstein condensate. *Phys. Rev. Lett.*, 85:483–486, 2000.

[5] Cheng Chin, Rudolf Grimm, Paul Julienne, and Eite Tiesinga. Feshbach resonances in ultracold gases. *Rev. Mod. Phys.*, 82:1225–1286, 2010.

[6] SL Cornish, NR Claussen, JL Roberts, EA Cornell, and CE Wieman. Stable Rb-85 Bose-Einstein condensates with widely tunable interactions. *Phys. Rev. Lett.*, 85(9):1795–1798, 2000.

[7] B DeMarco and DS Jin. Onset of Fermi degeneracy in a trapped atomic gas. *Science*, 285(5434):1703–1706, 1999.

[8] Bo Gao. Analytic description of atomic interaction at ultracold temperatures. II. Scattering around a magnetic Feshbach resonance. *Phys. Rev. A*, 84:022706, 2011.

[9] Markus Greiner, Cindy A. Regal, and Deborah S. Jin. Emergence of a molecular Bose-Einstein condensate from a Fermi gas. *Nature*, 426(6966):537–540, 2003.

[10] S Inouye, MR Andrews, J Stenger, HJ Miesner, DM Stamper-Kurn, and W Ketterle. Observation of Feshbach resonances in a Bose-Einstein condensate. *Nature*, 392(6672):151–154, 1998.

[11] Karina Jimenez-Garcia. *Artificial Gauge Fields for Ultracold Neutral Atoms.* PhD thesis, Joint Quantum Institute, National Institute of Standards and Technology, and the University of Maryland, 2012.

[12] S. Jochim, M. Bartenstein, A. Altmeyer, G. Hendl, S. Riedl, C. Chin, J. Hecker Denschlag, and R. Grimm. Bose-Einstein condensation of molecules. *Science*, 302(5653):2101–2103, 2003.

[13] Wolfgang Ketterle and Martin W. Zwierlein. Making, probing and understanding ultracold Fermi gases. In *Ultracold Fermi Gases, Proceedings of the International School of Physics 'Enrico Fermi', Course CLXIV*, Varenna, 20-30 June 2006.

[14] Gregory O. Konstantinidis, Melina Pappa, Gustav Wikstroem, Paul C. Condylis, Daniel Sahagun, Mark Baker, Olivier Morizot, and Wolf von Klitzing. Atom number calibration in absorption imaging at very small atom numbers. *Central European Journal Of Physics*, 10(5):1054–1058, 2012.

[15] Lindsey J. LeBlanc. *Exploring many-body physics with ultracold atoms.* PhD thesis, University of Toronto, 2011.

[16] Y.-J. Lin, A. R. Perry, R. L. Compton, I. B. Spielman, and J. V. Porto. Rapid production of ^{87}Rb Bose-Einstein condensates in a combined magnetic and optical potential. *Phys. Rev. A*, 79:063631, 2009.

[17] M. Lysebo and L. Veseth. *Ab initio* calculation of Feshbach resonances in cold atomic collisions: *s*- and *p*-wave Feshbach resonances in $^6Li_2$. *Phys. Rev. A*, 79:062704, 2009.

[18] H.J. Metcalf and P. van der Straten. *Laser Cooling and Trapping.* Graduate Texts in Contemporary Physics. Springer New York, 1999.

[19] C. Monroe, E. Cornell, C. Sackett, C. Myatt, and C. Wieman. Measurement of Cs-Cs elastic scattering at T =30 μK. *Phys. Rev. Lett.*, 70:414–417, 1993.

[20] K. M. O'Hara, S. L. Hemmer, M. E. Gehm, S. R. Granade, and J. E. Thomas. Observation of a strongly interacting degenerate Fermi gas of atoms. *Science*, 298(5601):2179–2182, 2002.

[21] C. Regal and D. Jin. Measurement of positive and negative scattering lengths in a Fermi gas of atoms. *Phys. Rev. Lett.*, 90:230404, 2003.

[22] CA Regal, M Greiner, and DS Jin. Observation of resonance condensation of fermionic atom pairs. *Phys. Rev. Lett.*, 92(4), 2004.

[23] G. Reinaudi, T. Lahaye, Z. Wang, and D. Guéry-Odelin. Strong saturation absorption imaging of dense clouds of ultracold atoms. *Opt. Lett.*, 32(21):3143–3145, 2007.

[24] E Tiesinga, BJ Verhaar, and HTC Stoof. Threshold and resonance phenomena in ultracold ground-state collisions. *Phys. Rev. A*, 47(5, B):4114–4122, 1993.

[25] E Timmermans, P Tommasini, MS Hussein, and A Kerman. Feshbach resonances in atomic Bose-Einstein condensates. *Physics Reports-review Section Of Physics Letters*, 315(1-3):199–230, 1999.

[26] D.S. Durfee W. Ketterle and D.M. Stamper-Kurn. Making, probing and understanding Bose-Einstein condensates. In *Bose-Einstein condensation in atomic gases, Proceedings of the International School of Physics 'Enrico Fermi'*, Course CXL, 1999.

[27] R. A. Williams, M. C. Beeler, L. J. LeBlanc, K. Jiménez-García, and I. B. Spielman. Raman-Induced interactions in a single-component Fermi gas near an *s*-wave Feshbach resonance. *Phys. Rev. Lett.*, 111:095301, 2013.

[28] R. A. Williams, L. J. LeBlanc, K. Jimnez-Garca, M. C. Beeler, A. R. Perry, W. D. Phillips, and I. B. Spielman. Synthetic partial waves in ultracold atomic collisions. *Science*, 335(6066):314–317, 2012.

[29] Saijun Wu, Ying-Ju Wang, Quentin Diot, and Mara Prentiss. Splitting matter waves using an optimized standing-wave light-pulse sequence. *Phys. Rev. A*, 71:043602, 2005.

[30] M. W. Zwierlein, C. A. Stan, C. H. Schunck, S. M. F. Raupach, S. Gupta, Z. Hadzibabic, and W. Ketterle. Observation of Bose-Einstein condensation of molecules. *Phys. Rev. Lett.*, 91:250401, 2003.

[31] M. W. Zwierlein, C. A. Stan, C. H. Schunck, S. M. F. Raupach, A. J. Kerman, and W. Ketterle. Condensation of pairs of Fermionic atoms near a Feshbach resonance. *Phys. Rev. Lett.*, 92:120403, 2004.